Detection of tropical deforestation using ALOS-PALSAR

MartinWhittle[a], Shaun Quegan[a], Yumiko Uryu[b] , Michael Stüewe[b], Koko Yulianto[c]

a CTCD, University of Sheffield, Hicks Building, Hounsfield Rd, Sheffield S3 7RH
b WWF-Indonesia/WWF Deutschland, Kantor Taman A9, Unit A-1, Jl. Mega Kuningan Lot 8-9/A9, Kawasan Mega Kuningan, Jakarta 12950, Indonesia.
c. WWF-Indonesia, Kantor Taman A9, Unit A-1, Jl. Mega Kuningan Lot 8-9/A9, Kawasan Mega Kuningan, Jakarta 12950, Indonesia.

Abstract

Indonesia has one of the highest rates of deforestation in the world, leading to a significant impact on planetary carbon balance and loss of biodiversity. It also covers a vast and often inaccessible area frequently obscured by cloud, making accurate, timely monitoring of its forests difficult. Spaceborne Synthetic Aperture Radar (SAR) images are unhindered by cloud and can provide clear images whenever there is a satellite pass, hence provide a potentially important tool for monitoring forest changes. Over Sumatra, the JAXA Advanced Land Observing Satellite (ALOS) PALSAR L-band radar provides both ScanSAR HH polarisation with repeat images every 46 days, thus providing much more frequent clear imagery than other available rapid deforestation monitoring tools, and approximately annual Fine-Beam Dual (FBD) image pairs with HH & HV polarisations. Temporal analysis of ScanSAR images shows that deforestation in the Sumatran province of Riau can be identified by large values of the temporal standard deviation, but high detection rates are associated with high false alarm rates, particularly in swamp forest. There does not appear to be a reliable signature of the onset of forest disturbance in the ScanSAR time-series. Deforestation can also be detected with annual change measured in FBD data. The best performance is achieved by combining increases and decreases in both the HH and HV channels, since all four indicators of change are complementary. This indicates the variety of the processes that may be involved in assigning a physical basis to the radar signature of deforestation. Significant improvements in performance are possible by combining FBD and ScanSAR data, giving 70% detection of deforestation for a false alarm rate (detection of deforestation in undisturbed forest) of 20%. Error analysis based on (a) likely errors in the Landsat data used to provide a reference for deforestation and (b) differences between the times of acquisition of the Landsat data and the FBD data suggest that the true detection rate for the FBD data is underestimated. All the analysis in the paper uses fully automatic methods, but it is likely that false alarms in the ScanSAR data due to periodic flooding could be reduced by human inspection. The performance figures reported here could also be improved if knowledge about the locations of dry and swampy forest was included in the methodology.

Keywords: Forest monitoring, tropical deforestation, change detection, ALOS PALSAR

1. Introduction

The rate of tropical deforestation is reported to have decreased from 0.16 M km^2 yr^{-1} in the 1990s to 0.13 M km^2 yr^{-1} in the first decade of the 21st century (FAO 2010), but destruction of natural forest is still a major source of carbon dioxide emissions (estimated as 16% of the anthropogenic emissions since 2000; (Le Quéré 2010)) and a primary factor in loss of biodiversity. However, there is huge uncertainty in these estimates and the associated emissions (Achard et al. 2002; Houghton 2005a; Le Quéré 2010) Reducing this uncertainty is crucial to assessments of global carbon balance for climate modelling and harnessing political will for change. Current efforts to provide economic incentives to reduce deforestation through the United Nations Framework Convention on Climate Change Reduced Emissions from Deforestation and Degradation (REDD+) mechanism (Parker et al. 2009; UNFCCC 2007, 2011) are also dependent on reliable, independent estimations of deforestation rates (Goetz et al. 2009).

Indonesia is one of the few remaining countries in the world with extensive natural forest cover and associated biodiversity, but has one of the world's highest rates of forest loss and associated greenhouse gas emissions from forest degradation and loss. According to (Hansen et al. 2009; Hansen et al. 2008), Indonesia's current deforestation rate of 3.4% per year is second only to that of Brazil among countries with humid tropical forests. Deforestation in Indonesia ranges from selective logging to large-scale clearance for pulp wood and agricultural plantations. Given the vast and remote areas, efficient monitoring of these losses must depend on satellite-based techniques. However, (Fuller 2006) contrasts the success of forest monitoring in Brazil with the situation in Indonesia, where inadequate monitoring and a lack of transparency and accountability has created an urgent need for independent verification.

Remote sensing of forest disturbances using optical, short-wave or near-infrared reflectance and thermal spectra is well established (Fuller 2006; Hais et al. 2009), but in tropical regions its usefulness is frequently limited by haze from forest fires and cloud cover, especially during the seasonal monsoon. Synthetic Aperture Radar (SAR), operating at microwave frequencies, is not hampered by this problem and allows regular long-term monitoring (Podest and Saatchi 2002).

The Japanese Aerospace Exploration Agency (JAXA) Advanced Land Observing Satellite (ALOS) (Rosenqvist et al. 2007) became fully operational in June 2006 and includes a Phased Array L-band Synthetic Aperture Radar (PALSAR) operating at 1270 MHz (a wavelength of 26.4 cm) that provides a number of image products. In this paper we investigate the effectiveness of ScanSAR and Fine Beam Dual (FBD) images, both separately and in combination, for monitoring tropical deforestation. ScanSAR images typically cover 359 km in range and 379 km in swath, i.e. 136000 km^2, and are acquired with the same geometry once every 46 days, hence are well suited to monitoring large regions for changes associated with deforestation. FBD images consist of image pairs at HH & HV polarisation, with dimension 69.8 km in range by 58.6 km in azimuth, with repeat images usually acquired at 3 times a year during June, July and September. Hence they lack the time or space coverage of ScanSAR, but the HV channel is expected to give significant advantages for detection of deforestation (Leckie and Ranson 1998).

The principal objective of this paper is to assess the ability of ALOS-PALSAR to monitor tropical deforestation using a case study in Sumatra. This is addressed in three stages:

1. Development of methods to detect changes associated with deforestation in ScanSAR data, and evaluation of whether 46-day HH data allows accurate detection of the onset of deforestation. This is to assess whether ScanSAR data can be used to trigger rapid response to illegal logging (as in the MODIS-based Brazilian DETER system [www.obt.inpe.br/deter]).
2. Development of methods to detect deforestation in time-separated FBD images, and evaluation of whether they lead to acceptable performance for deforestation detection.
3. Evaluation of whether combining FBD and ScanSAR yields superior results.

The methods developed are intended to allow ALOS-based forest monitoring to be carried out in a scientifically robust manner, preferably at technician level. A broader goal is to provide the Indonesian and global community with tools for using ALOS-PALSAR data that allow transparent, accurate and frequent tracking of natural forest cover change, independently of cloud and haze, and that can be used as a basis for action on forest carbon management and biodiversity conservation. The knowledge gained by this activity should also contribute towards a better understanding of the land carbon cycle.

Because this study has strong implications for potential uses of ALOS-PALSAR in monitoring tropical forests (for example, in REDD or through the Group on Earth Observations Forest Carbon Tracking initiative [http://www.geo-fct.org/]), we give a thorough description of the methods and our efforts to optimise them. We provide quantitative assessment of ScanSAR alone, FBD alone and their combined use to detect deforestation, and discuss the accuracy of these assessments, given uncertainties in the data used to test them. Our conclusions summarise the results, and indicate further work needed to assess their wider significance in the monitoring of tropical deforestation.

2. Data

2.1 Study area: ground and satellite data coverage

Sumatra has the most intense recent large-scale forest clearance in Indonesia, with the province of Riau recording the highest degree of change (Hansen et al. 2009). A very detailed land cover database for the Riau & Jambi regions, based on Landsat imagery for 2007, was provided by WWF (Uryu et al. 2007). This distinguishes 49 types of land cover, including dry lowland forest, mangrove forest, peat-swamp forest and swamp forest types. Each of these four types of natural forest is subdivided into three levels of cover, designated as rather closed canopy, medium open canopy and very open canopy. A second WWF database, derived from Landsat imagery in 2008 and 2009, is less detailed, but delineates natural forest and non-natural forest regions over a smaller area partially overlapping the 2007 database (Uryu et al. 2010). To use both databases, we amalgamated land cover into just nine classes (see Table 1), which included two types of natural forest, "dry" and "swampy" (usually peat swamp), derived from the WWF 2007 database. The natural forest indicated as lost between the 2007 and 2008 databases is used as our reference for deforestation. All the accuracy analysis in this paper is based on the assumption that the databases themselves are accurate, but Section 5 discusses the effects of relaxing this assumption.

Table 1 Land cover types in the amalgamated WWF databases

Land cover Types
Natural forest (swampy)
Natural forest (dry)
Shrub, grass, fern
Regrowth (all types, including forest, shrubs, semak, belukar muda)
Plantation (rubber, oil palm, acacia, coconut)
Paddy fields
Water
Agricultural (mixed agriculture, mixed garden)
Cleared (cleared post-acacia, harvested, etc).

This study uses a set of twelve ScanSAR images, centred on 1.728° S, 102.332° E (Path 115, Frame 3650), that cover much of the intersection of the two WWF land-cover databases. The supplied data were processed by JAXA at the 1.5 level (which includes radiometric correction, range and multi-look azimuth compression, geocoding and orthorectification) and were converted to intensity with GAMMA software (http://www.gamma-rs.ch/) using the standard calibration factor of -83 dB (Rosenqvist et al. 2007). The images are HH-polarised with 100 m × 100 m pixel spacing across a swath of width 359 km and along-track dimension 379 km. The incidence angle varies from 18.0° to 43.0° across the swath. All the images have the same geometry and form an unbroken sequence with 46-day temporal separation running from 31/01/2007 to 20/06/2008. We also analysed FBD images from path 443, frame 7170, acquired on 28/06/2007 and 30/06/2008, which cover part of the ScanSAR scene; these are referred to as FBD-1 and FBD-2 respectively. In addition, a third FBD image (FBD-3; Path 443, Frame 7180) acquired on 30/09/2008 lying just to the north of FBD-1&2 is used in Section 4.3. The FBD data are HH-HV image pairs, also processed at the 1.5 level, with 12.5 m × 12.5 m pixel spacing and incidence angle from 36.6° to 40.9°. The swath width is 69.8 km and the along-track dimension 58.6 km.

The acquisition dates of the various satellite images contributing to this study are given in Fig. 1. Fig. 2a shows the coverage of the databases and the ScanSAR images, with the common overlap between all three types of data indicated by a yellow outline. This overlap, which has a total area of 2428358 ha, will be referred to as region "Y". Also shown is the area covered by the FBD images within region Y. Fig. 2b shows the distribution of dry and swampy forest in region Y, together with the areas deforested between 2007 and 2008 in each type of forest. Natural forest accounts for 979159 ha (40.3%) of region Y in the WWF 2007 database; of this, 151380 ha (15.5% of the forest area) had been deforested by 2008. Approximately 64.1% of the original forest area consisted of dry forest while 35.6% was swampy. The 0.3% discrepancy arises at region margins where pixels are sometimes classified as both types. This can happen when the borders between regions defined by vector graphics bisect pixels in raster-based images.

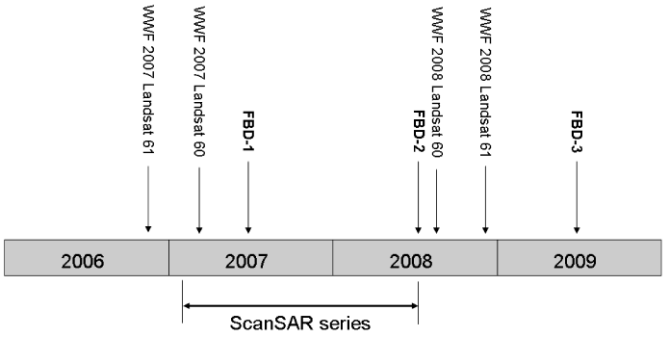

Fig. 1. Acquisition timeline for satellite data used in this study. The 12 ScanSAR images were acquired at intervals of 46 days between 31/01/2007 and 20/06/2008. The three FBD images were obtained on 28/06/2007, 30/06/2008 (P443, F7170) & 30/09/2008 (P443, F7180). For the WWF databases, the study area is covered by Landsat images for path 126, rows 60 and 61 (indicating position in the azimuth direction). For the 2007 database they were acquired on 23/04/2007 for row 60 and 14/11/2006 for row 61; the corresponding dates for the 2008 database were 22/07/2008 and 24/09/2008 respectively.

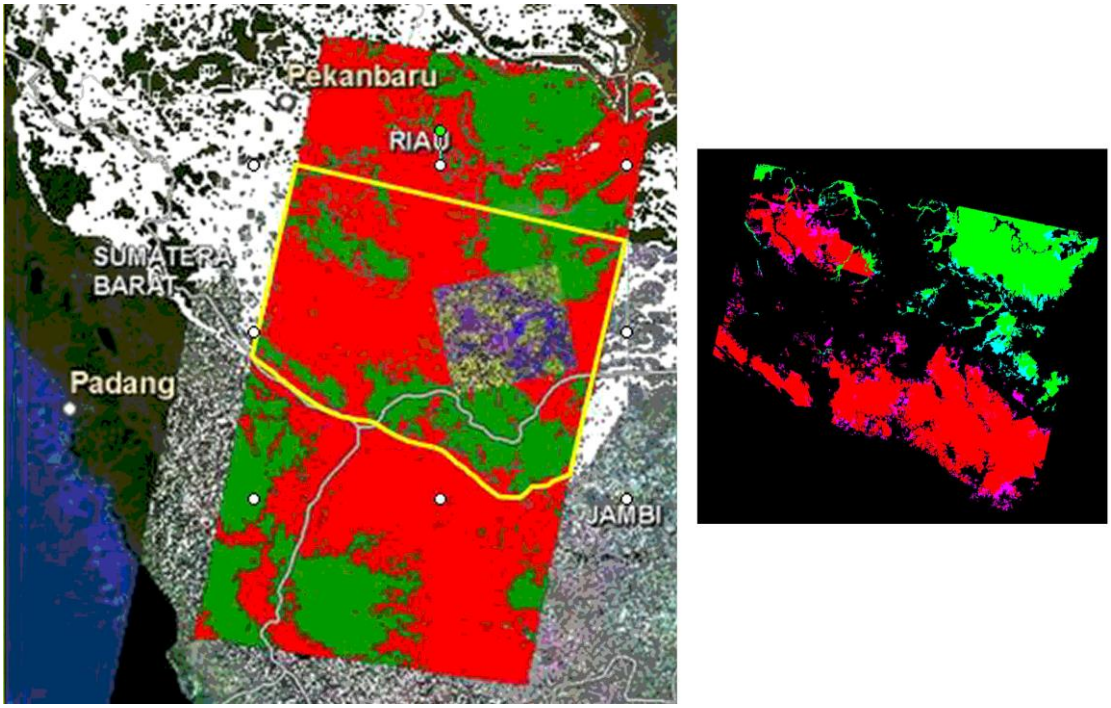

Fig. 2. (left) Part of a ScanSAR image of the Riau and Jambi regions of Sumatra overlaid by the WWF 2007 land-cover database (shown with white outlines) and the WWF 2008 database (the large rectangle, in which green and red parts indicate natural forest and non-forest respectively). The ScanSAR image is a RGB composite of images acquired in Jan. 2007, Sept. 2007 and June 2008. The two databases and the ScanSAR footprint intersect in the region Y outlined in yellow. Enclosed by region Y is the FBD scene discussed in section 4.2, shown as a RGB composite of the HH and HV channels and the HH/HV ratio; (right) RGB image showing the areas of natural forest and deforestation derived from the 2007 and 2008 databases in region Y. Red and green indicate dry and swamp forest respectively. Regions deforested in the interval between construction of the two databases are shown as pink and light blue in the dry and swampy areas respectively.

3. Methods

3.1 Pre-processing of the time-series of ScanSAR data

The detection of deforestation relies on observing change over time, and requires some basic pre-processing. The ScanSAR images were first co-registered using GAMMA software. A multi-channel filter (Quegan and Yu 2001) was then applied with window size 5×5 to reduce speckle; this increased the estimated equivalent number of looks from 6.7 for an unfiltered image to 31.9 for each of the filtered ScanSAR images. The whole image sequence could then be compared at the pixel level. Initial comparisons revealed that the mean backscatter from the forest regions varied by almost 2 dB over the 18-month period, as shown in Fig. 3. The highest values occur in the images acquired on 31/01/2007 and 19/12/2007, corresponding to the seasonal high monsoon rainfall between November and March (200-300 mm/month), while the lowest values occur for the images acquired on 03/08/2007 and 20/06/2008 in the

"dry" season (75-150 mm/month). Fig 3a and 3b differ in that the areas used to measure the forest backscatter are taken from the 2007 and 2008 databases respectively.

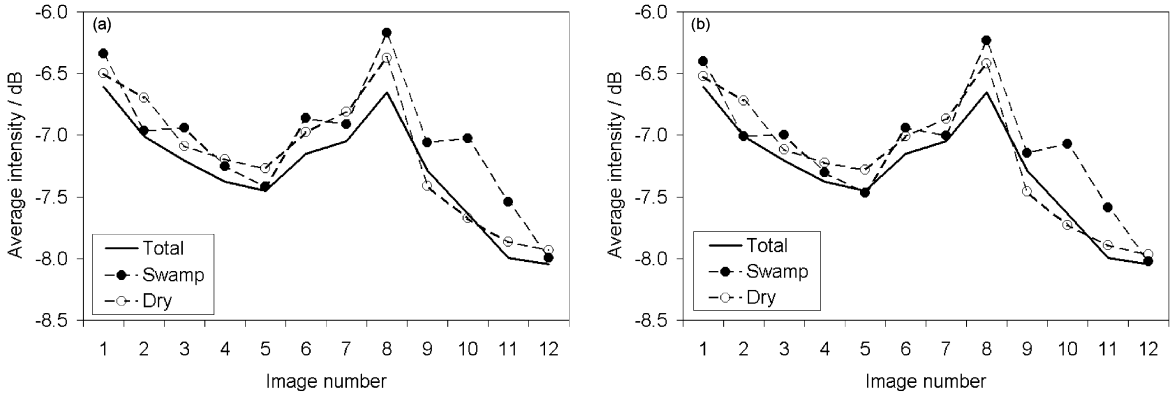

Fig. 3. Average intensity as a function of time for the whole ScanSAR scene (─), and for the areas of swamp (-●-) and dry forest (-○-); the forest values are derived from (a) the 2007 WWF database, and (b) the 2008 WWF database.

It is necessary to remove these trends in order to detect local intensity changes that are caused by deforestation and are of comparable magnitude. This was achieved by rescaling the data so that the mean forest intensity in each image became equal to the time-average of the overall mean forest intensity, i.e. all pixels in the k^{th} image were multiplied by the factor $\bar{I}_f / \bar{I}_f(k)$, where $\bar{I}_f(k)$ is the mean forest intensity in the k^{th} image and $\bar{I}_f$ is the overall mean forest intensity obtained by averaging these values. The forest area used was that in the 2007 database; although this area shrunk by ~15.5% in the interval between the formation of the databases, Fig. 3 shows that this makes little difference to the normalisation. Hence use of the known forest prior does not lead to any significant bias.

Fig. 4 shows time-series of such normalised data in areas designated as deforested (Fig. 4a-b) and in undisturbed natural forest (Fig. 4c-e). The time-series for each pixel in a 5×5 window is shown, with the mean and the mean ±1 standard deviation (SD) of the overall forest intensity indicated as horizontal lines. Fig. 4a shows a large increase in backscatter (up to ~3.14 dB) associated with deforestation, but deforestation can also occur without sharp changes or significant variation in backscatter (Fig. 4b). Similarly, very different types of behaviour can occur in undisturbed forest, from significant trends and variability (Fig. 4c-d) to little change (Fig. 4e).

3.2 General change detection measures

C- and L-band HH measurements in temperate and boreal regions have indicated that forest areas tend to exhibit more stable backscatter than other land cover types (Quegan et al. 2000). Hence it was expected that general change detection methods would be effective in detecting the presence of deforestation in the ScanSAR time-series, before more detailed analysis locating the onset of the event within the series. The change measures considered were:

Range: $$I_{max}(\mathbf{x}) - I_{min}(\mathbf{x}) \qquad (1)$$

SD: $$SD(\mathbf{x}) = \left[\frac{1}{N-1} \sum_{i=1}^{N} \left(I(\mathbf{x}, t_i) - \mu(\mathbf{x}) \right)^2 \right]^{\frac{1}{2}} \qquad (2)$$

Mean absolute variation from the mean: $$AD(\mathbf{x}) = \frac{1}{N}\sum_{i=1}^{N}\left| I(\mathbf{x},t_i) - \mu(\mathbf{x}) \right| \quad (3)$$

Mean absolute inter-image variation: $$Vm(\mathbf{x}) = \frac{1}{N-1}\sum_{i=1}^{N-1}\left| I(\mathbf{x},t_{i+1}) - I(\mathbf{x},t_i) \right| \quad (4)$$

Maximum inter-image change: $$I_{\max c}(\mathbf{x}) = \max_{1\le i\le N-1}\left[I(\mathbf{x},t_{i+1}) - I(\mathbf{x},t_i) \right] \quad (5)$$

Minimum absolute inter-image change: $$I_{\min c}(\mathbf{x}) = \left| \min_{1\le i\le N-1}\left[I(\mathbf{x},t_{i+1}) - I(\mathbf{x},t_i) \right] \right| \quad (6)$$

where $I_{max}(\mathbf{x})$ and $I_{min}(\mathbf{x})$ are the maximum and minimum intensity values in the time-series at position **x,** $\mu(\mathbf{x}) = \frac{1}{N}\sum_{i=1}^{N} I(\mathbf{x},t_i)$ is the temporal mean intensity at position **x,** and the images were acquired at times t_i, i = 1-N. In addition, at each pixel we measured the net change in intensity from its initial value:

$$I_{sum}(\mathbf{x}) = \sum_{i=2}^{N}\left[I(\mathbf{x},t_i) - I(\mathbf{x},t_1) \right] = \sum_{i=2}^{N} I(\mathbf{x},t_i) - (N-1) I(\mathbf{x},t_1). \quad (7)$$

The distribution of values for any of these measures can be summarised by a probability density function (PDF) and the corresponding cumulative frequency distribution (CFD). Examples of the PDFs and CFDs for the temporal SD of deforested areas and natural forest are shown in Fig. 5; they are calculated over the WWF 2007 forest region within the region Y shown in Fig. 2.

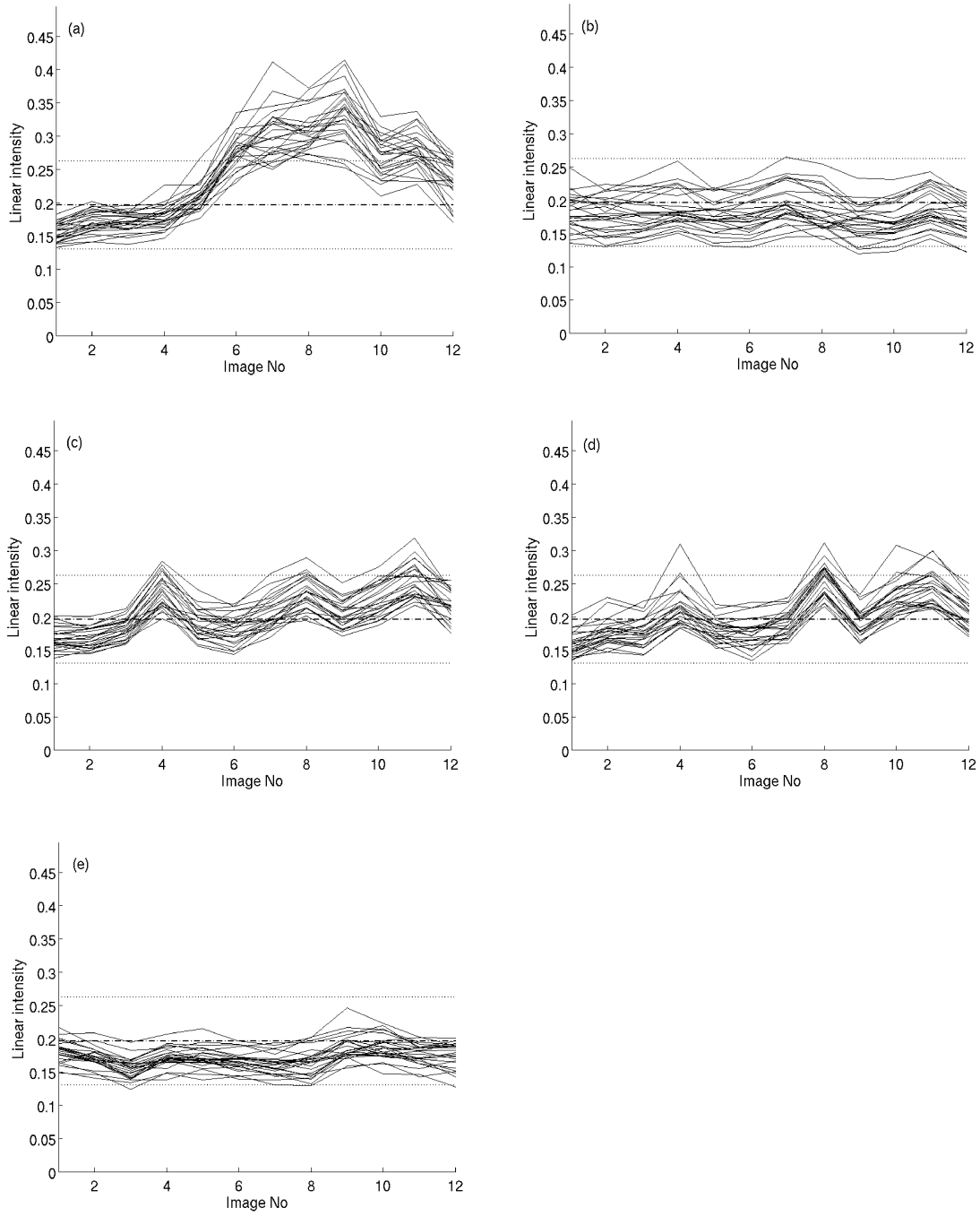

Fig. 4. ScanSAR time-series for each pixel in a set of 5×5 windows located in areas undergoing deforestation (Fig. 4a-b) and undisturbed forest (Fig. 4c-e). The horizontal dot-dash lines indicate the mean overall forest intensity and the dotted lines show 1 SD on either side.

From the CFDs we can find the proportion of pixels whose value exceeds a given threshold and hence, for any fixed threshold, the probability detection for deforestation, P_d, and the false alarm probability for undisturbed forest, P_{fa}. The use of an approach based on detection concepts rather than classification is more appropriate for deforestation, which is normally a rare event (though in region Y, 15.5% of the natural forest is lost in the period between the formation of the two databases). Bayesian methods therefore strongly weight the

classification towards undisturbed forest, and typically would fail to classify any of the pixels as deforested (this would be the case for the PDFs shown in Fig. 5).

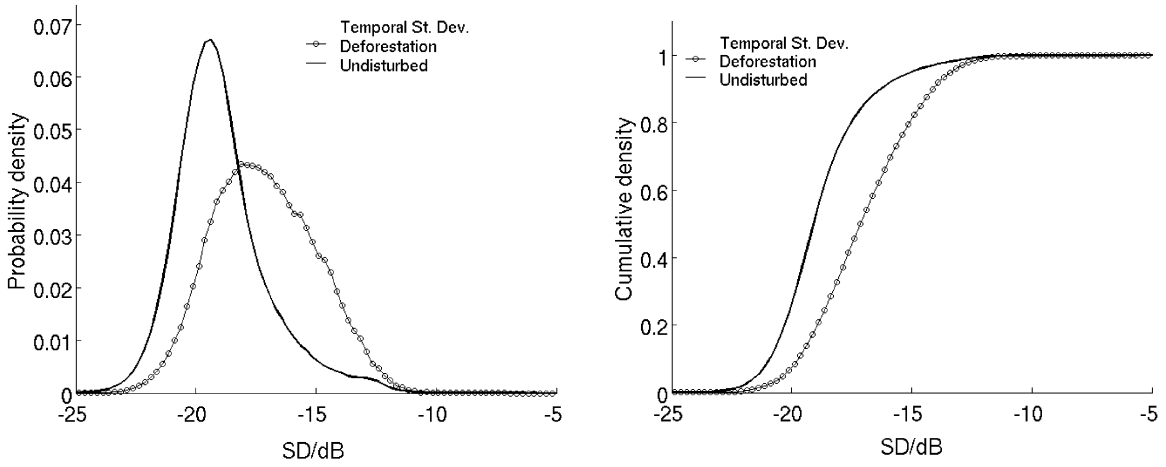

Fig. 5. (a) PDFs of the temporal SD in undisturbed forest (─) and deforested regions (-○-); (b) the corresponding CFDs .

A useful way to assess detection performance is through the "receiver operating characteristic" (ROC) curve, which plots P_d against P_{fa}; each point on this curve corresponds to a particular threshold value. ROC curves for the various change measures are given in Fig. 6. These demonstrate that, except at unacceptably low detection probabilities, the temporal SD gives the highest detection rate for a given false alarm rate (although the range measure gives almost the same performance). The change measures are highly correlated, so combining them (for example using Principal Component Analysis) does not improve the performance achieved by the temporal SD alone. This single measure of change is therefore adopted in the rest of the paper.

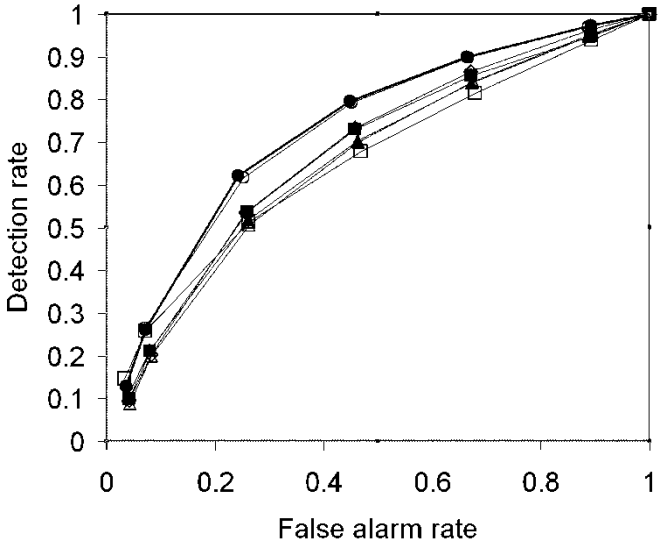

Fig. 6. ROC curves for the following change measures: *SD* ─●─; σ_{max} ─■─; $(I_{max}–I_{min})$ ─○─; *Vm* ─◊─; I_{maxc} ─▲─; I_{minc} ─Δ─; $|I_{sum}|$ ─□─.

3.3 Measuring change in FBD images

This study uses pairs of FBD multi-channel filtered intensity images of the same scene gathered approximately a year apart to measure change in forest regions. As for ScanSAR (Section 3.1), the images were first normalised to the same average forest intensity: all pixels in the k^{th} image (k = 1, 2) were multiplied by $\bar{I}_f / \bar{I}_f(k)$, where $\bar{I}_f(1)$ and $\bar{I}_f(2)$ are the average forest intensities of images acquired at times t_1 and t_2, and $\bar{I}_f$ is their mean, i.e. the overall average forest intensity This was carried out separately for the HH and HV images.

Change detection is based on image ratios, for which accurate results require the data to be heavily averaged (Rignot and van Zyl 1993); we use 23×23 averaging windows, for reasons discussed in Section 4.2. We consider two change measures, $I_2(\mathbf{x})/I_1(\mathbf{x})$, which is positive (negative) if intensity increases (decreases), and one which combines both sorts of change:

$$R_1(\mathbf{x}) = \max\left[\frac{I_1(\mathbf{x})}{I_2(\mathbf{x})}, \frac{I_2(\mathbf{x})}{I_1(\mathbf{x})}\right] - 1. \qquad (8)$$

The value of R_1 is zero if there is no change and otherwise is positive; statistics of a related measure using the *min* operator are discussed in (Touzi et al. 1988). For simplicity, throughout the paper we use the same notation, $I_k(\mathbf{x})$, for both the original data and normalised, window-averaged data.

4. Results

4.1 Detecting deforestation using ScanSAR data

As indicated by Fig. 6, choice of a threshold on the temporal SD fixes the detection and false alarm probabilities. Images showing true detections and false alarms for the forested areas in region Y are shown in Fig. 7a and 7b for false alarm rates of 23.6% and 6.8% respectively (corresponding to the 30th and 10th percentiles respectively). The northern part of the forest area in Fig. 7a has a high proportion of false alarms clustered around the point marked Location A (0° 16’ 25.32’’ S, 102° 58’ 12.636’’ E) and along the adjoining river valley. This region is designated as swamp forest in the WWF 2007 database, and a ground survey on 18th June 2009 confirmed it to be a frequently flooded peat swamp forest with very open canopy containing palm, pandan and rattan. The temporal sequence of backscatter at point A is plotted in Fig. 4c, while Fig. 4d shows the sequence for a point about 1.7 km to the south-west that could not be reached by the surveyor because of flooding and dense vegetation.

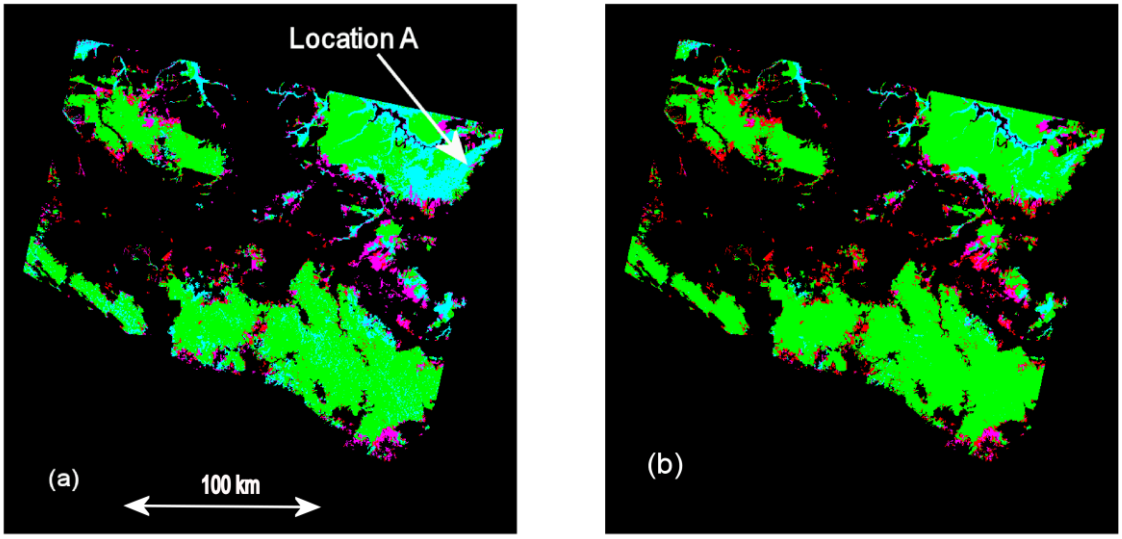

Fig. 7. Images of the forest areas in region Y, with the red and green channels assigned to pixels that were respectively deforested and undisturbed between 2007 and 2008, according to the WWF databases. The blue channel is assigned to pixels whose temporal SD exceeds a threshold corresponding to false alarm rates of (a) 23.6% and (b) 6.8%. Thus magenta indicates true detection of deforestation and light blue indicates false alarms in undisturbed forest. Location A gives the approximate location of a point that was ground surveyed.

4.1.1 Dry and swampy forest regions

The study area contains dry and swampy forest. When undisturbed, both have average intensities of about -7 dB, but dry forest exhibits higher spatial variability: the average of the SDs of spatial intensity in the 12 images is 0.0720 (-11.4 dB) for dry forest and 0.0526 (-12.8 dB) for swamp forest. In contrast, temporal variability is greater in swamp forest, as shown by the PDFs of temporal SD in Fig. 8a (here the total PDFs for undisturbed forest and deforestation are the same as those in Fig. 5a). It can be seen that:

- The modal value for deforested pixels is significantly higher in swamp forest than dry forest, so the detection rate in swamp forest will be larger for a given total false alarm rate;
- Although the mode for undisturbed forest is similar for the two types, the swamp forest distribution has a long positive tail, causing proportionally more false alarms.

ROC curves derived separately for swamp forest, dry forest and total forest are shown in Fig. 8b. The two types of forest exhibit significant differences, e.g. at 10% false alarm rate, the detection probability for dry forest is roughly twice that for swampy forest, but these correspond to different thresholds. Use of a single threshold based on total P_{fa} therefore gives different performance in dry and swamp forests and ideally separate thresholds should be set for swamp and dry forest, if these forest types can be delineated (as in our case).

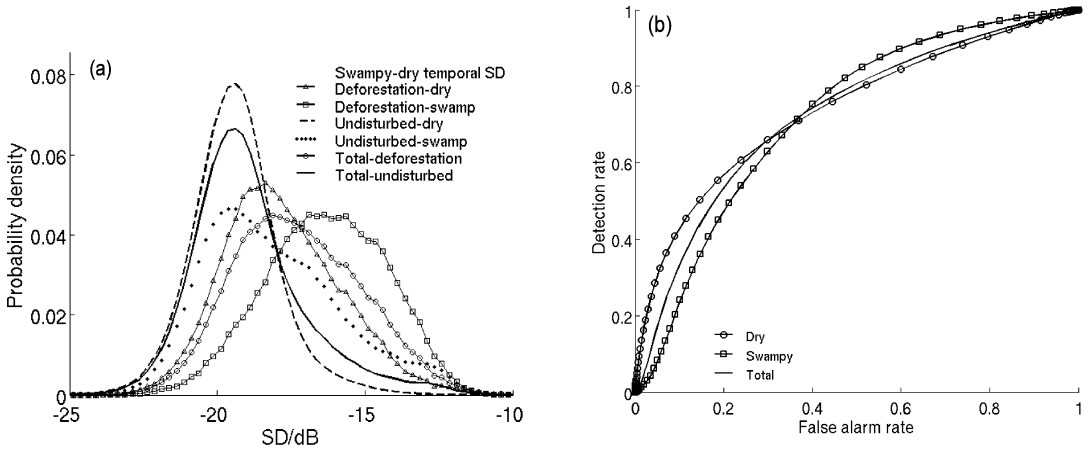

Fig. 8. (a) PDFs of temporal SD calculated for undisturbed forest and deforested regions: total undisturbed ──; total deforested ─○─; dry undisturbed - - -; dry deforested ─Δ─; swampy undisturbed • • • ; swampy deforested ─□─. (b) The associated ROC curves for (−○−) dry, (─□─) swamp and (□□) total forest areas.

4.2 Detecting deforestation using FBD data

Detection of change based on ratios of FBD intensity images from different times (equivalent to differences of dB images) is discussed in section 3.3. Fig. 9 shows PDFs for the ratio $R(\mathbf{x}) = I_1(\mathbf{x})/I_2(\mathbf{x})$ of images I_1 and I_2 acquired on 28/06/2007 and 30/06/2008, respectively, for the FBD scene shown as the inset in Fig. 2, in which 2590280 deforested pixels and 6096144 undisturbed pixels are recorded in the databases. Separate PDFs are shown for undisturbed and deforested areas, and for the HH and the HV images. Surprisingly, the modal value in all four distributions is nearly zero, and the differences between undisturbed and deforested regions only emerge in the tails. For both HH and HV, the PDFs for deforestation are wider and show that both increases and decreases in intensity are associated with deforestation.

The importance of considering both types of change is clear from Fig. 10, which covers a portion of the scene measuring 40 km × 36 km. For both HH and HV, the pixels lying in the top 10% of the ratios I_2/I_1 and I_1/I_2 are displayed in red, those in the 10 – 20% range in green, and those in the 20 – 30% range in blue. Figs. 10a and 10b indicate increases over time in HH and HV, while Figs. 10c and 10d indicate decreases. Fig. 10e is a fused result discussed in Section 4.2.1, while Fig. 10f shows the areas of deforestation and undisturbed forest derived from the WWF databases. It is clear that:

- the HH and HV data both contribute to overall detection of deforestation;
- increases are as important as decreases in detecting deforestation;
- changes in HH and HV complement each other, despite some overlap.

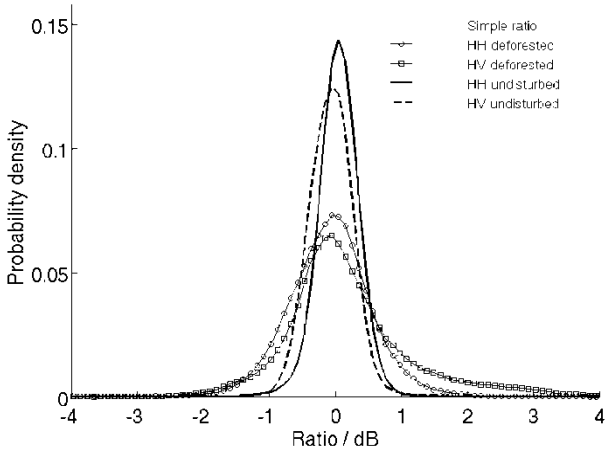

Fig. 9. PDFs of I_1/I_2 for scenes acquired on 28/06/2007 and 30/06/2008. Separate PDFs are shown for undisturbed (□□) and deforested (−○−) regions in HH and undisturbed (- - -) and deforested (─□─) regions in HV.

The degree of overlap between the HH and HV changes shown in Fig. 10 can be quantified using the Simpson coefficient (Holliday et al. 2003); for two classes containing *k* and *l* pixels whose overlap contains *m* pixels, this is given by:

$$S_{sim} = \frac{m}{\min(k,l)}. \qquad (9)$$

This expresses the overlap as a fraction of the smallest class; complete overlap of either class by the other yields a value of unity. The Simpson coefficients for HH and HV changes at the 10^{th} and 20^{th} percentiles are given in Table 3, in which the 20% range includes the 10% range.

Table 3. Simpson coefficients for overlap of the four types of change at the 10% and 20% level for increases and decreases of the HH and HV channels.

Change		Increase	Decrease
		HV10	HV10
Increase	HH10	0.271	0.013
Decrease	HH10	0.072	0.321
		HV20	HV20
Increase	HH20	0.311	0.056
Decrease	HH20	0.128	0.336

The highest value in the table is 0.336; hence, although there is some overlap between the four types of detection, they are significantly different, even when they have the same sign. The values in the leading diagonals are notably larger than the off-diagonal terms, showing that changes of the same sign in HH and HV are more closely associated than changes of opposite sign; nonetheless, it can be seen that at the 20% level, the set of pixels for which HV increases overlap those where HH decreases at the 0.13 level. Hence all four types of change are needed to build up a deforestation map.

4.2.1 Combining FBD change measures

A first step in combining the different types of change is to use the generalised change measure R_1 defined in eq. (8), which incorporates both increases and decreases of intensity. ROC curves were used to establish the optimum averaging window before forming ratios; this emerges clearly from Table 4, which shows the detection rate for deforestation under a false alarm rate of 20% for different window sizes. It can be seen that:

- detection rates increase with the size of the window, up to a side-length of 23 pixels, then stabilise;
- although the HH detection rate is lower for smaller windows, it approaches that for HV as the window gets bigger, and both channels give similar performance once the window size reaches 23x23 pixels (corresponding to a side-length of 287.5 m);
- using larger windows does not improve the performance in HV and only slightly improves the performance in HH.

This motivates the use of 23x23 averaging windows for FBD data throughout the paper.

Table 4 Detection rates against window size for the HH and HV channels for $P_{fa} = 0.2$.

Window side-length (pixels)	HH	HV
1	0.32	0.37
5	0.36	0.43
11	0.43	0.49
17	0.49	0.52
23	0.51	0.54
29	0.53	0.54
35	0.54	0.54

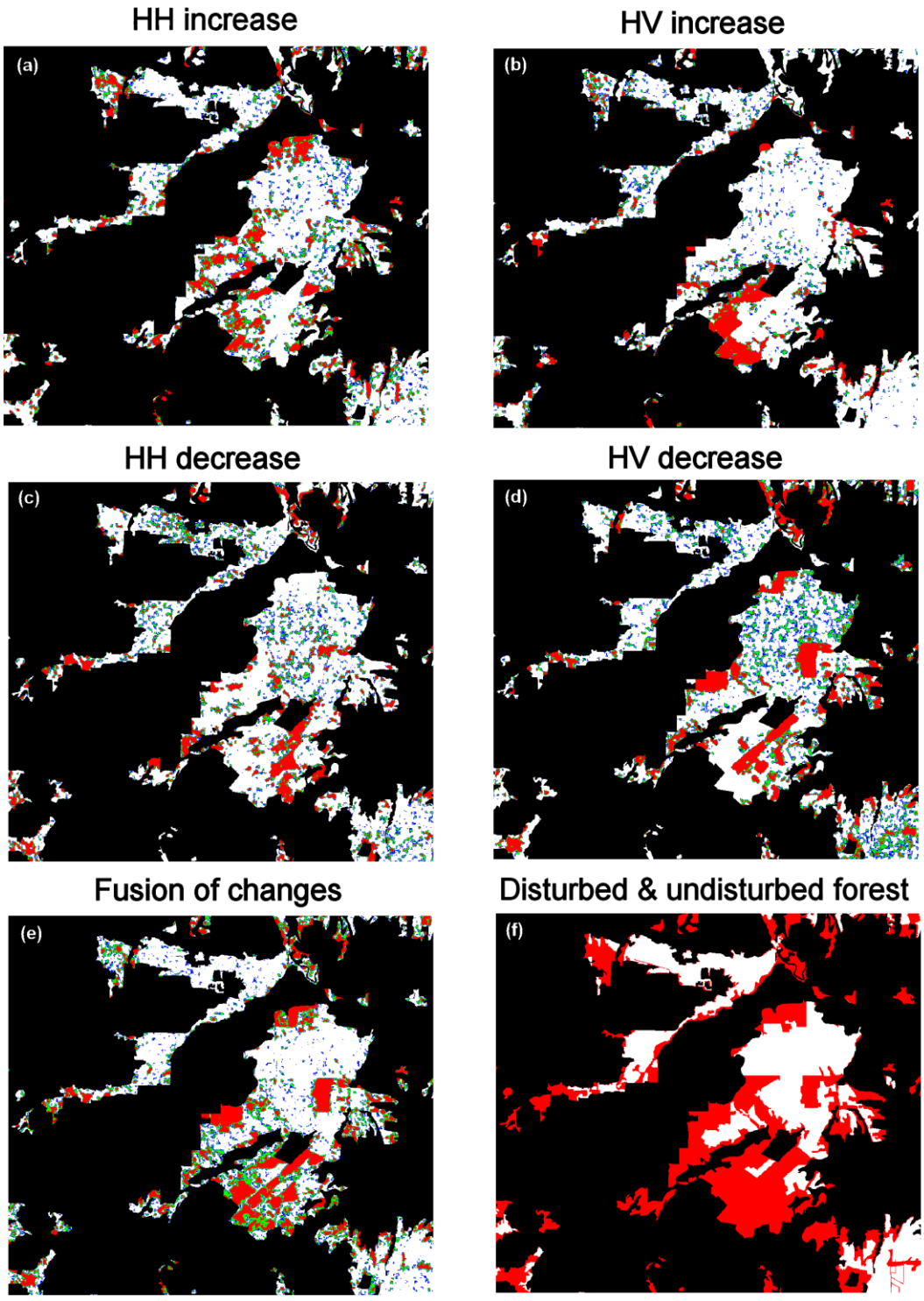

Fig. 10. A portion of the FBD scene measuring 40 km × 36 km; pixels whose FBD temporal ratio, measured in the undisturbed natural forest in the 2007 database, lies in the top 10%, 10-20% & 20-30% percentile ranges are marked in red, green and blue respectively. Non-forest is shown black. (a) HH increase; (b) HV increase; (c) HH decrease; (d) HV decrease; (e) the combined result using data fusion; (f) undisturbed natural forest (white) and deforested areas (red) derived from the WWF databases.

PDFs of R_1 for deforested and undisturbed forest areas are shown in Fig. 11. Many deforested pixels exhibit low values of R_1, but the higher values can separate deforested from undisturbed regions. Detection and false alarm rates when the R_1 values for HH and HV are thresholded at the 10% and 20% levels are given in Table 5. This shows that HH gives fewer detections and more false alarms than HV at both the 10% and 20% level. However, HH and HV pick out significantly different pixels, as evidenced by the Simpson coefficient; the overlap in HH and HV gives a value of 0.34 for thresholding at the top 10% level, and 0.39 for the top 20%. Thus combining HH and HV change should yield better performance.

Various combination methods were investigated. The most effective on this dataset ranked the values of R_1 for HH and HV separately, then assigned to each pixel the higher of the HH and HV rankings (Ginn et al. 2000); this is denoted as *maxr*. However, at 20% P_{fa}, this gave less than 1% higher detection rate than the simple average, R_{1av}, of the R_1 values for each channel, and for other datasets the results for R_{1av} were slightly better than those for *maxr*. Hence, as R_{1av} is simpler to use, we adopted it as the means to combine the HH and HV data. ROC curves for R_1 for each channel and their combination, R_{1av}, are shown in Fig. 12a.

Table 5 Detection and false alarm rates when the R_1 values for HH and HV are thresholded at the 10% and 20% levels.

	HH10	HV10	HH20	HV20
P_d	0.254	0.283	0.408	0.433
P_{fa}	0.032	0.020	0.107	0.096

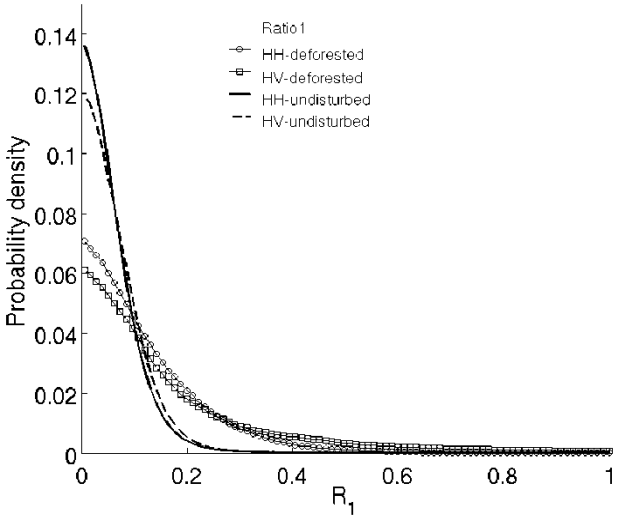

Fig. 11. PDFs of R_1 for HH in undisturbed (□ □) and deforested (−○−) regions and for HV in undisturbed (- - -) and deforested (─□─) regions.

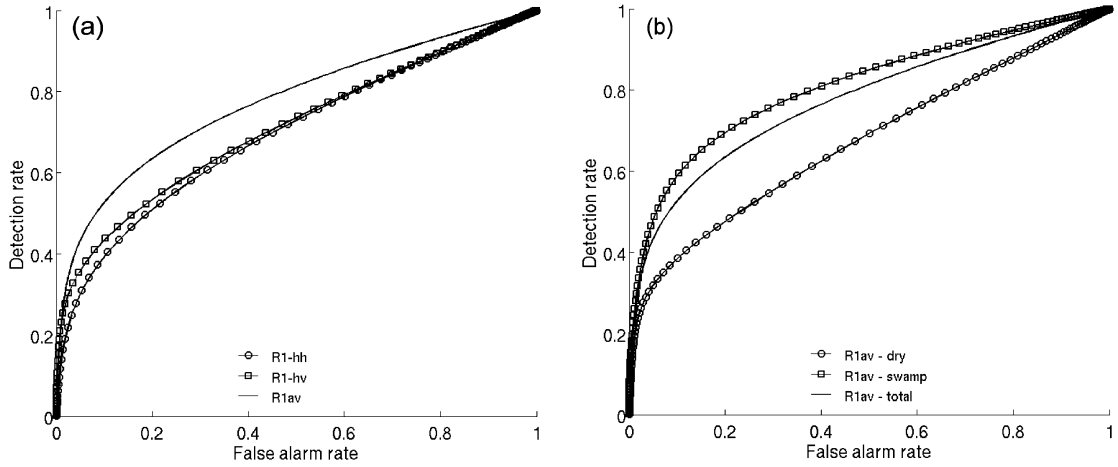

Fig. 12. (a) HH (−○−) and HV (─□─) ROC curves for the total forest region in the FBD scene obtained by thresholding R_1, and the combined result obtained by using R_{1av} (──); (b) ROC curves obtained using R_{1av} for swampy forest (─□─), dry forest (−○−) and total forest (□□). The curves for R_{1av} in (a) and R_{1av} total forest in (b) are the same.

Three key points emerge from Fig. 12a:

1. HH gives a lower detection rate than HV for a given false alarm rate, but the difference decreases as the false alarm rate increases; at a false alarm rate of 20%, 51.0% of the deforestation is detected using HH and 53.5% using HV.
2. At 20% false alarm rate, the single-channel detection rates are comparable with ScanSAR (see Fig. 8b).
3. Combining the HH and HV detections gives a detection rate of 63.5% at a false alarm rate of 20%, which is ~10% greater than detection using HV alone.

Fig. 12b shows that much better performance is found for swampy forest than for dry forest in the combined detection scheme, as long as separate detection thresholds are applied to the two types of forest; this is the opposite of what was observed for ScanSAR (see Fig. 8b). If no *a priori* knowledge of the geographical locations of the two types of forest is available, an overall threshold will have to be chosen, and the performance will depend on the proportions of swamp and dry forest in the scene.

The WWF databases also distinguish "closed" and "open" forest types, and differences were found between them: the detection probability was ~3% greater for closed forest than for open forest at a false alarm rate of 20%, and ~7% for a false alarm rate of 5%.

4.3 Comparing FBD and ScanSAR detections

FBD and ScanSAR ROC curves for the forest areas in the whole of the FBD scene are shown in Fig. 13a and 13b. For FBD (Fig. 13a), a 30% threshold on R_{1av} gives a detection rate of 60.2% with a false alarm rate of 16.4%, while the same threshold on the ScanSAR temporal SD (Fig. 13b) detects 56.7% of the deforested regions with a false alarm rate of 17.8%. Hence, FBD data yield both a higher detection rate and lower false alarm rate than ScanSAR for thresholding at this percentile. In contrast, a 30% threshold applied to the ScanSAR temporal SD over the whole of region Y detects 62% of the deforested regions with a false alarm rate of 23.8% (Fig. 13c). (Note that the normalisation of the ScanSAR data [see Section 3.1] was matched to the scene considered.) Such differences between scenes are to be

expected when an overall threshold is applied, since detection and false alarm rates are different for swamp and dry forest; hence the overall detection and false alarm rates will depend on the relative proportions of these forest types in the scene.

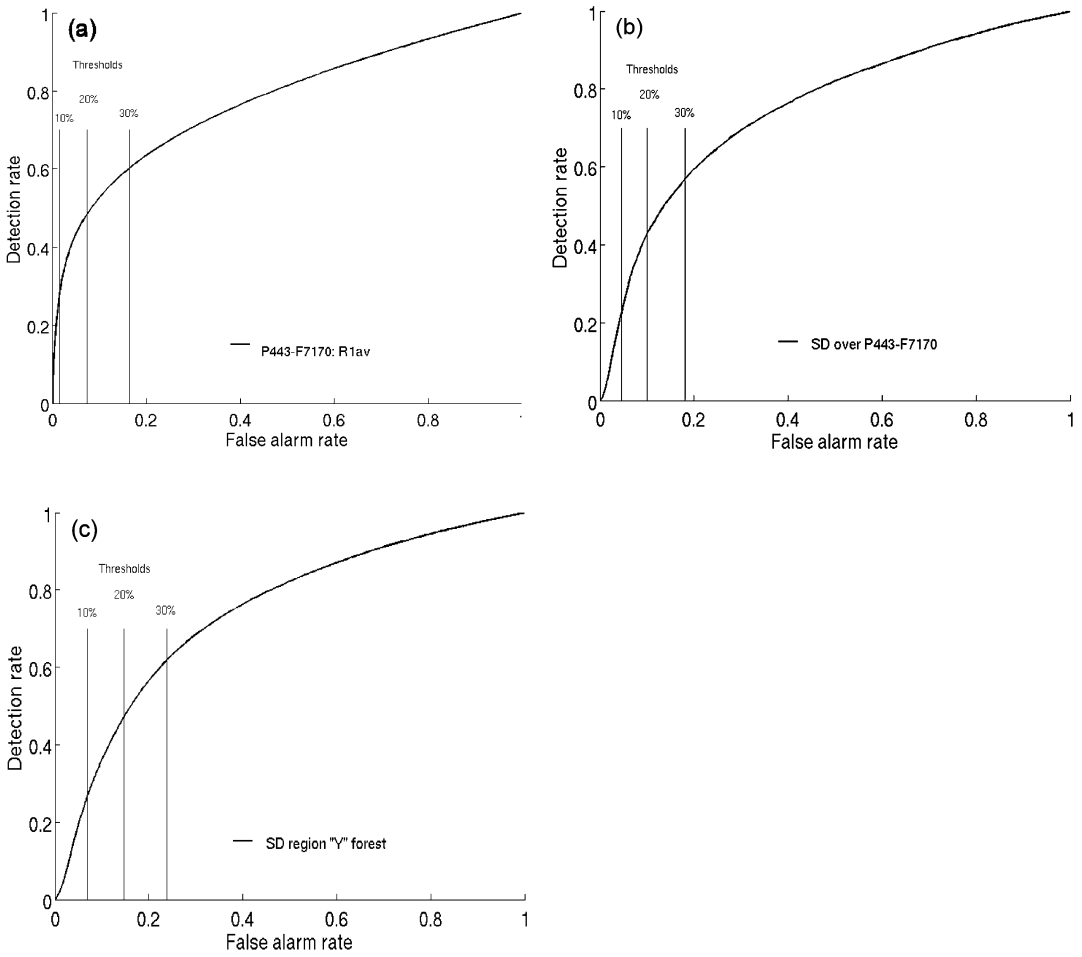

Fig. 13. ROC curves for: (a) R_{1av} over the FBD footprint; (b) ScanSAR temporal SD over the FBD footprint; (c) ScanSAR temporal SD over region Y. The 10%, 20% and 30% thresholds are indicated by vertical bars.

A notable feature of ScanSAR false alarms is that they often occur along watercourses and, in these cases, are likely to be caused by signal variations associated with flooding. An example is shown in Fig. 14, where ScanSAR detections (marked with white shading) and deforestation derived from the databases (in red) are overlaid on a section of the FBD-3 scene, which is displayed with HH, HV and HH/HV assigned to red, green and blue respectively. The same region can be seen some 50 km WNW of location A in Fig. 7a. It is well-known that forest inundation often gives rise to major increases in L-band HH backscatter due to a sharp increase in the double-bounce mechanism, and this has been used to monitor the annual cycle of flooding in tropical forest regions (Martinez and Le Toan 2007). For a human interpreter, both context and the cyclical nature of these types of false alarm allow them to be readily recognised. However, we have not yet developed automatic methods to identify them, and they contribute to our estimates of false alarm rate.

4.4 Combining FBD and ScanSAR data for detection of deforestation

Sections 4.1-4.3 have investigated the individual abilities of ScanSAR and FBD data to detect deforestation and compared them. However, the two types of detection use very different properties of the PALSAR data, so in this section we investigate whether gains can be made by combining them. Because ScanSAR data are supplied at a different resolution and orientation to FBD data, they were first re-sampled and co-registered with the FBD data using ENVI software (http://www.ittvs.com/).

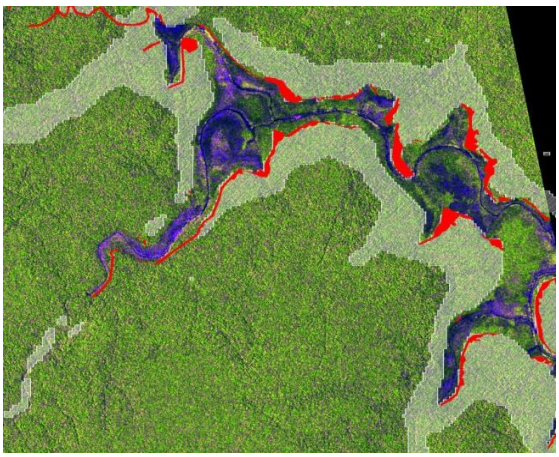

Fig. 14. Overlay of ScanSAR detections using a 10% threshold (hatched in white) and database-derived deforestation (in red) on a section of FBD-3 measuring 18.5×14.6 km that covers a region of swampy forest. The HH, HV and HH/HV data in the FBD image take the red, green and blue channels respectively.

ScanSAR temporal SD and FBD $R_{1\mathrm{av}}$ have different ranges, but they can each be mapped to a value between 0 and 1 by the transformation

$$\hat{A}(\mathbf{x}) = \frac{A(\mathbf{x}) - A_{\min}}{A_{\max} - A_{\min}} \tag{10}$$

where $A_{\max}$ and $A_{\min}$ are the maximum and minimum values of the measure A over the region (Whittle et al. 2004). The transformed values of $R_{1\mathrm{av}}$ and ScanSAR temporal SD are denoted as $\hat{R}_{1\mathrm{av}}(\mathbf{x})$ or $\hat{S}_D$ respectively, and the quantity *sums* is then defined by:

$$sums(\mathbf{x}) = \hat{R}_{1\mathrm{av}}(\mathbf{x}) + \hat{S}_D(\mathbf{x}). \tag{11}$$

Other combined measures considered included taking the maximum value of $\hat{R}_{1\mathrm{av}}(\mathbf{x})$ and $\hat{S}_D(\mathbf{x})$, and forming measures that first ranked the pixels in each data type separately, then assigned to each pixel the maximum or the sum of the two ranks. None of these out-performed *sums*.

The ROC curves for $R_{1\mathrm{av}}$ and *sums* over the FBD footprint are shown in Fig. 15a. Combining ScanSAR with FBD data gives some improvement over FBD alone, but significant increases in detection rate only occur for false alarm rates around 20% or larger. A visual impression of the effects of combining the data types is given by Fig. 16a-c, where detections over the FBD footprint using $R_{1\mathrm{av}}$, ScanSAR temporal SD and *sums* at the 10%, 20% and 30% threshold levels are indicated by red, green and blue respectively. The data combination suppresses several of the small noise-like areas in the bottom left of the scene that are detected in the FBD data with a 30% threshold (compare Fig. 16a and 16c). Also apparent is that the large area right of top centre detected by ScanSAR at the 10% level is reduced in size using the

combined measure, but the remnant has little overlap with the deforested area indicated by the databases, Fig. 16e. Since this area is associated with a river valley, it is likely to be a manifestation of ScanSAR erroneously detecting inundation as deforestation, as discussed in Section 4.3.

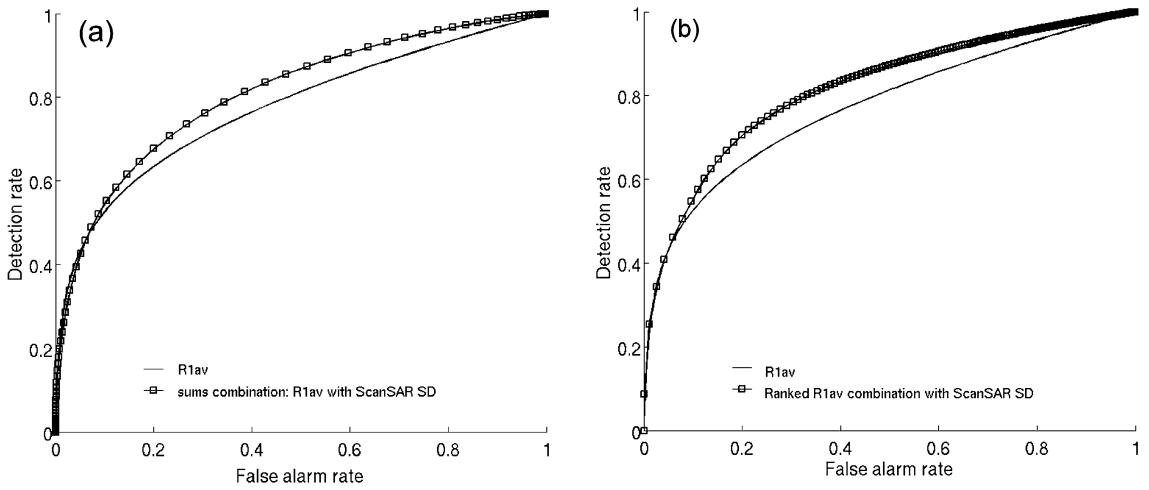

Fig. 15. ROC curves for: (a) R_{1av} (□) and the combined FBD-ScanSAR measure *sums* (-□-); (b) R_{1av} (□) and the combined FBD-ScanSAR measure *comb* (-□-). The curves for R_{1av} are identical to that shown in Fig. 13a and are calculated over the FBD footprint.

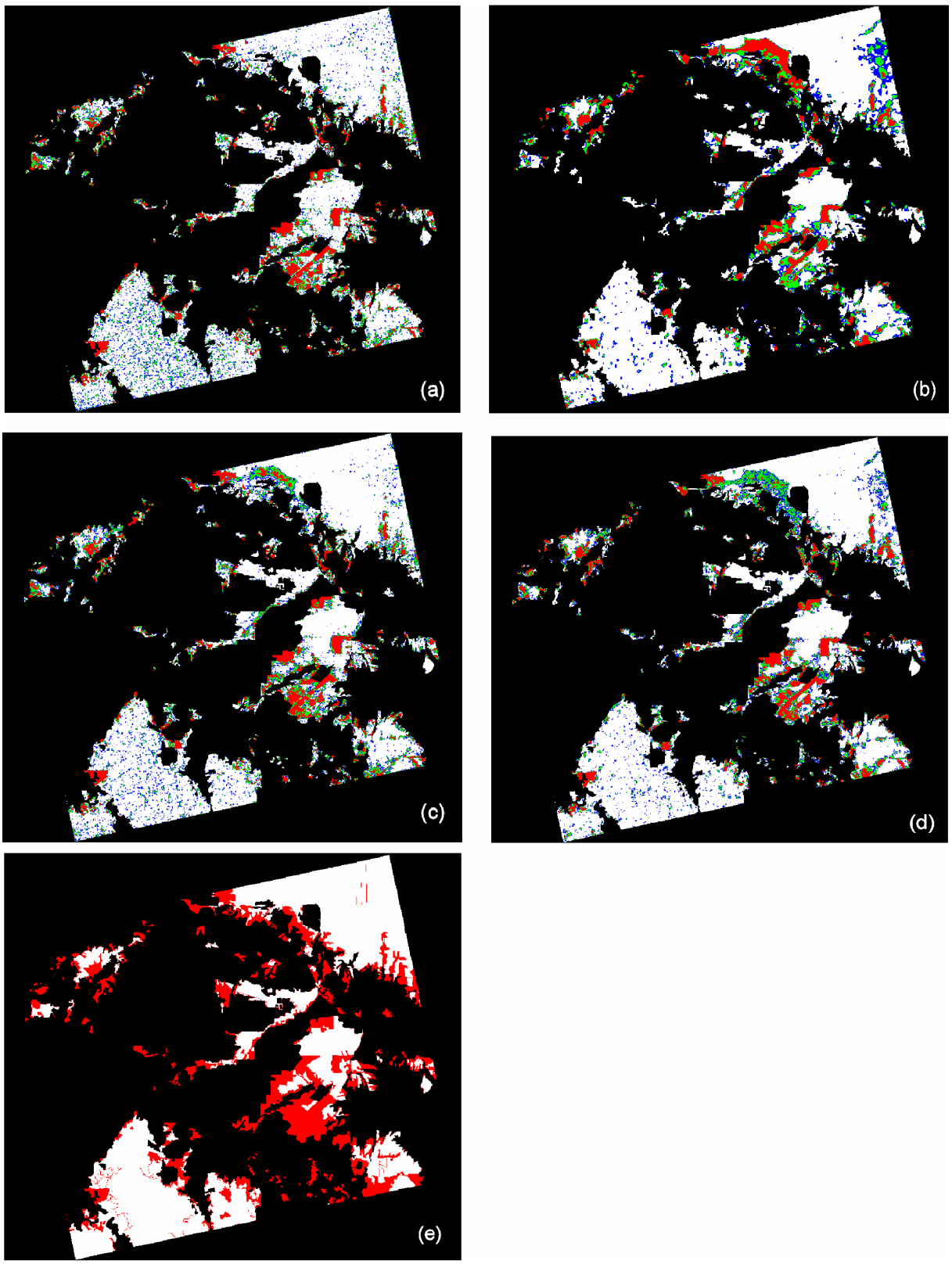

Fig. 16. Detection of deforestation over the FBD footprint using: (a) R_{1av}; (b) the ScanSAR temporal SD; (c) the combined measure *sums*; (d) the combined measure *comb*. (e) Undisturbed forest (white) and deforested areas (red) derived from the WWF databases. For (a)-(d), red, green and blue indicate pixels in the top 10%, 10-20% and 20-30% ranges respectively.

The combined measure *sums* gives equal weights to $\hat{R}_{1\mathrm{av}}$ and $\hat{S}_D$, but other linear weightings could be used. However, these are unlikely to improve performance. Heavier weighting towards $\hat{R}_{1\mathrm{av}}$ would reduce the small gains from including ScanSAR shown in Fig. 16c. Heavier weighting towards $\hat{S}_D$ would increase the false alarm rate due to moisture effects. We therefore developed a non-linear method of combining the data that combines $R_{1\mathrm{av}}$ with ScanSAR detections (rather than original values of the ScanSAR temporal SD). The procedure adopted was to form three masks with pixel values 0 or 1, where 1 was assigned to values in the top 10%, 10-20% and 20-30% ranges of ScanSAR temporal standard deviation over the FBD footprint; these masks are referred to as SC09, SC08 and SC07 respectively. These were then combined into a single image, S, containing only the discrete values 0.7, 0.8, 0.9 and 0, using the expression

$$S = 0.7 * SC07 + 0.1 * SC08 + 0.1 * SC09. \tag{12}$$

Detection based on percentiles relies only on the ordering of values, so the FBD data were first ranked, and the ranks were divided by the total number of pixels to give a value, $\breve{R}_{1av}$, between 0 and 1. The *comb* measure was then defined by:

$$comb = \breve{R}_{1av}(1 - S) + S \tag{13}$$

Since S can only take the four values 0, 0.7, 0.8 and 0.9, *comb* can be thought of as four linearly increasing functions of $\breve{R}_{1av}$ that take the value 1 if $\breve{R}_{1av}$ = 1 and S if $\breve{R}_{1av}$ = 0. Pixels whose ScanSAR temporal SD is small are strongly discriminated against for detection unless their values of $\breve{R}_{1av}$ are very high.

An ROC curve for *comb* is shown in Fig. 15b, where it is compared with the ROC curve for $R_{1\mathrm{av}}$. The detection rate at a false alarm rate of 20% is 70.5%, while the corresponding values for *sums* for $R_{1\mathrm{av}}$ alone are 67.7% and 63.5% respectively. Hence this method leads to useful improvement in performance. Note, however, that neither combined method gives better detection rates than $R_{1\mathrm{av}}$ alone for false alarm rates below ~0.1. The benefits of using *comb* are illustrated by the map of detections shown in Fig. 16d. This shows strong suppression of the noise-like regions detected in the lower left of Fig. 16a (using FBD alone) and in the FBD-ScanSAR combination using *sums* (Fig. 16c). The erroneous ScanSAR detections right of top centre are still present but at a lower level of confidence. Comparison with Fig. 16e shows that, out of the three measures, *comb* gives the best correspondence between detections and the WWF database information. However, it must be noted that *comb* is not based on an optimisation principle and is to some extent empirically-based. Nonetheless, it illustrates two key points: (1) useful improvements in detection performance can be made by combining ScanSAR with FBD data; (2) the optimum approach will require a non-linear method of combining ScanSAR and FBD measurements.

5. Accuracy of the WWF databases

The quantitative analysis in this paper has assumed that the deforestation inferred from the WWF 2007 and 2008 databases accurately represents the changes occurring over the period observed by the radar images. However, this may be incorrect, for two reasons:

1. There may be errors in the databases. Uncertainties in the Landsat classification of deforested areas have previously been noted for a study in the Brazilian Amazon(Houghton 2005b; Houghton et al. 2000).
2. Deforestation may have occurred between the dates of the Landsat images used to derive the 2007 database and the first FBD scene, or the dates of the second FBD image and the Landsat images used to derive the 2008 database.

The latter would have larger effects on the FBD data analysis, because the ScanSAR series begins much earlier than the first FBD image (Fig. 1).

For FBD data, both sources of error can be accounted for by expressing the estimated values of P_d and P_{fa} in terms of their true values; these are given by (see Appendix for details):

$$\hat{P}_d = \frac{P_d\ f_D(t_1,t_2) + P_{fa}\left(f_D(t_2,t_3) + (1 - f_D(t_0,t_3))Y\right) + P_p(DF \mid NF)\left(f_D(t_0,t_1) + X\right)}{X + Y + f_D(t_0,t_3)(1-Y)} \tag{14}$$

and

$$\hat{P}_{fa} = \frac{P_d\, f_D(t_1,t_2)V + P_{fa}\left(1 - f_D(t_0,t_3) + f_D(t_2,t_3)V\right) + P_p(DF \mid NF)\left(f_D(t_0,t_1) + X\right)V}{1 + XV + f_D(t_0,t_3)(V-1)} \tag{15}$$

where $f_D(t_i,t_j)$ is the fraction of the forest area deforested between times t_i and t_j, and $P_p(DF \mid NF)$ is the probability that a pixel is detected as deforestation even though it was non-forest on both the two acquisition dates of the FBD data. This false alarm probability is needed because some areas of non-forest could have been erroneously assigned to forest in the Landsat classification. Also,

$$X = \frac{A_{NF} P_L(F \mid NF)}{A_F P_L(F \mid F)},$$

$$Y = \frac{P_L(NF \mid F)}{P_L(NF \mid NF)},$$

$$V = \frac{P_L(F \mid NF)}{P_L(F \mid F)},$$

where $P_L(F \mid NF)$ denotes the probability that a Landsat pixel is classified as forest given that it is non-forest, and $P_L(F \mid F)$, $P_L(NF \mid F)$ and $P_L(NF \mid NF)$ are defined similarly. A_F and A_{NF} are the areas of forest and non-forest at the time of formation of the 2007 WWF database, t_0. The times t_1, t_2 and t_3 denote the date of the first FBD acquisition, the second FBD acquisition and the time of formation of the 2008 WWF database respectively. Then

$$P_d - \hat{P}_d = \frac{(P_d - P_{fa})\left(f_D(t_2,t_3) + (1 - f_D(t_0,t_3))Y\right) + (P_d - P_p(DF \mid NF))\left(f_D(t_0,t_1) + X\right)}{X + Y + f_D(t_0,t_3)(1-Y)} \tag{16}$$

and

$$\hat{P}_{fa} - P_{fa} = V\,\frac{\left(P_d - P_{fa}\right) f_D(t_1,t_2) + \left(P_p(DF \mid NF) - P_{fa}\right)\left(f_D(t_0,t_1) + X\right)}{1 - f_D(t_0,t_3) + V(X + f_D(t_0,t_3))} \tag{17}$$

Hence $P_d > \hat{P}_d$ as long as P_d exceeds both the false alarm rates. If the time effects can be neglected, so that $f_D(t_0,t_1) = f_D(t_2,t_3) = 0$ and $Y << 1$, then

$$P_d - \hat{P}_d = \frac{(P_d - P_{fa})(1 - f_D)Y + (P_d - P_p(DF \mid NF))X}{X + Y + f_D} \tag{18}$$

where $f_D = f_D(t_0, t_3)$. In this expression a critical factor is the size of f_D relative to *X* and *Y*. If it is comparable to or smaller than these terms then P_d can differ significantly from its estimate. If, instead, it is significantly larger than these terms, then $\hat{P}_d$ will be a good estimate of P_d. For the area considered in this study, f_D ~ 15.5%, and this condition is likely to hold.

Turning now to the false alarm rate, its true value will be less than its estimate as long as P_{fa} is less than both P_d and $P_p(DF \mid NF)$; otherwise, it can be less than or greater than its estimate, depending on the sizes of the different terms involved. However, the quantity *V* is expected to be small, and the ratio it is multiplied by will be less than 1 except under very unusual circumstances; as a result, $\hat{P}_{fa}$ is likely to be a good estimate of P_{fa}. Hence, for this dataset, errors in the Landsat classification are unlikely to cause large errors in the estimates of either the detection or false alarm rates derived for the FBD data. However, for other datasets, where the fractional area deforested is substantially smaller than here, significant errors in estimates of the detection rate can be caused if Landsat data are used as the reference.

If the errors due to Landsat misclassification are very small, i.e. $X = Y = V \sim 0$, then eqs. (14) and (15) reduce to

$$\hat{P}_d = \frac{P_d\ f_D(t_1, t_2) + P_{fa}\ f_D(t_2, t_3) + P_p(DF \mid NF)\ f_D(t_0, t_1)}{f_D(t_0, t_3)} \tag{19}$$

and

$$\hat{P}_{fa} = P_{fa}. \tag{20}$$

Hence only the detection probability is affected by the differences between the acquisition dates of the FBD data the Landsat images used to form the WWF databases. We can see from Fig.1 that this is likely to be more serious at the start of the period (from t_0 to t_1) since the interval between the last Landsat image used to form the WWF database and the first FBD image is several months.

Evidence for errors caused by such time differences is illustrated in Fig. 17. This shows colour composites of the centre right of the region shown in Fig. 16 for FBD data from 28/06/2007 (Fig. 17a) and 30/06/2008 (Fig. 17b), together with an overlay of the database estimate of deforestation, hatched in white, on the second FBD image (Fig. 17c). Forest canopy tends to depolarise the scattered signal (Leckie and Ranson 1998) and give enhanced HV backscatter, so is likely to comprise the area in green. It is clear that large areas indicated as deforested by the WWF databases, i.e. classified as forest in the earlier database and as non-forest in the later one, were already deforested by the time of the first FBD acquisition. Expressed in terms of the quantities in eq. (19), this means that $f_D(t_0, t_1)$ cannot be neglected and $f_D(t_1, t_2) < f_D(t_0, t_3)$, so that our estimates of $\hat{P}_d$ may be significantly less than the true P_d. Also shown in Fig. 17d is a Landsat-5 image from 20/06/2008, which was not used in constructing the 2008 database. It is unusually free of cloud and shows some important differences from the second FBD image, which was acquired only 10 days later. Most obvious is the anvil-shaped region in centre left, which Landsat clearly indicates to be a

disturbed region, but is practically invisible in the FBD data (though there are signs of disturbance on its left side in the earlier FBD image). This region is detected, at least partly, by ScanSAR (see Fig.7) and in the combination based on *comb* (Fig. 16d). Both the Landsat and FBD images show row structures in the forest; these indicate drainage channels that are a precursor to deforestation.

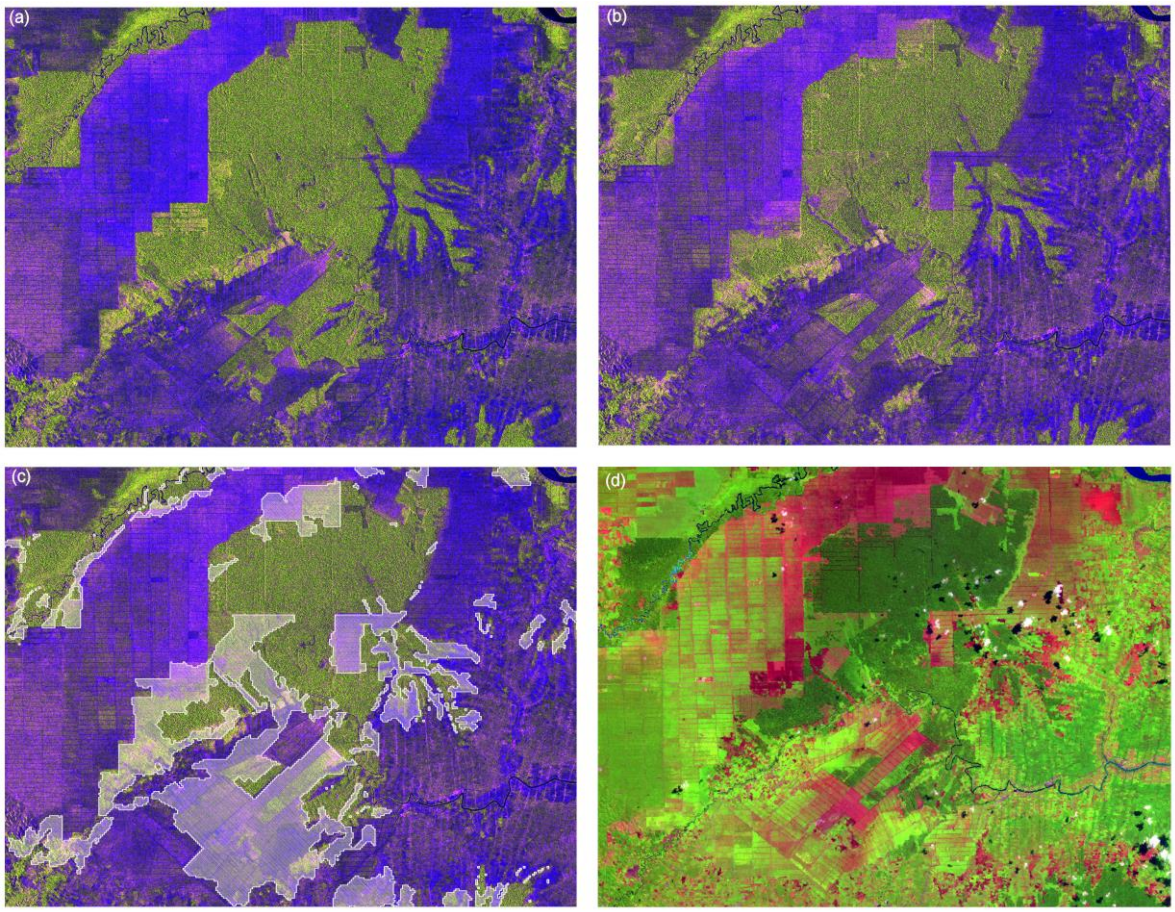

Fig. 17. (a) FBD image composite, with HH, HV and HH/HV taking the red, green and blue channels respectively, over a part of the area displayed in Fig. 10, for data acquired on 28/06/2007. (b) As (a), but for 30/06/2008. (c) Image (b) overlaid by the database estimate of deforestation, hatched in white. (d) Part of an unusually cloud-free Landsat-5 image for the same region acquired on 20/06/2008 displayed as a RGB composite using channels 3, 4 and 5.

6. Discussion

This paper provides a thorough investigation of the strengths and limitations of ScanSAR and FBD data, used separately or in combination, in detecting deforestation in Sumatra. It has shown that the frequently-held assumption of the primary importance of HV compared with HH is not so clear in this dataset, and that expected indicators of deforestation (reduced HH and HV backscatter) form only part of the measurements needed to achieve optimum detection of deforestation. It also makes clear that ALOS-PALSAR achieves its best performance when FBD is fused with ScanSAR in the detection process. Key conclusions are:

1. Deforestation does not leave a distinctive signature in ScanSAR data. Increases, decreases and more general types of change are all encountered when deforestation occurs. This is consistent with observations of both increases and decreases in L-band backscatter associated with deforestation in the Amazon (Angelis et al. 2002; Stone and Woodwell 1988). Hence isolating the start of a deforestation event by trying to fit some characteristic profile of change is not effective, except in a limited number of cases. More useful are general measures of change, with temporal standard deviation proving the most effective. This yields detection rates of 38% and 56% for false alarm rates of 10% and 20% respectively.
2. The detection performance of ScanSAR is greatly hampered by the great variability of backscatter in the remaining natural forest in this region, especially swamp forest. This means that acceptably low false alarm rates can only be achieved at the expense of reduced detection rates.
3. The best results for detection of deforestation in FBD data exploit both increases and decreases in HH and HV intensity, since the four types of change carry complementary information. Contrary to expectations, the detection performance with HH alone is only slightly worse than with HV alone, but significantly better results are obtained by combining them. Detection rates for HH, HV and the combination of HH & HV were found to be respectively 39%, 43% and 53% for a false alarm rate of 10% and 51%, 54% and 64% for a false alarm rate of 20%.
4. Of the types of change in FBD data caused by deforestation, only the decreases in HV and HH have ready explanations. The first is expected because forest canopies tend to depolarise the radar signal, giving a strong HV signal that is lost when deforestation occurs. For HH, canopy scattering tends to be greater than surface scattering except for very rough surfaces (where roughness is measured relative to the wavelength), so deforestation would be expected to reduce the HH signal. Explaining increases in the HV and HH signals is more speculative. Increased HV implies increased depolarisation, which could be induced by randomly oriented forest detritus left after deforestation. Because of the long wavelength, this would require relatively large tree components, such as secondary branches, to be left after deforestation, otherwise they would scatter too little power; this effect is therefore dependent on management practices. Explanation of the increases in the HH signal also seems to rely on material left after deforestation. If only a small amount of material is left and this consists of twigs and leaves, the dominant scattering mechanism would be surface scattering, which would tend to be specular and give low return because of the long wavelength. Hence an increase in HH requires larger types of material to be left, which effectively forms a very rough surface, giving increased backscatter. The spatially varying nature of these different types of change (see Fig. 10) presents problems in designing field studies to identify the physics of what is happening.
5. ScanSAR and FBD respond to different properties of the scene and the best detection performance is obtained by combining both. This yields detection rates of 56% for a false alarm rate of 10% and 70% for a false alarm rate of 20%; the corresponding detection rates using only the FBD $R_{1\mathrm{av}}$ measure are 53% and 64% respectively.
6. The detection rates given in points 2, 3 & 5 are scene-dependent, since performance is different for wet and dry forests, and the setting of an overall detection threshold would be affected by the proportion of each type of forest in the scene. If information is available on the geographical distribution of each type of forest in the scene, the detection scheme could be improved by applying different thresholds to each forest type.
7. Use of differences between forest maps derived from Landsat data to quantify the accuracy of deforestation estimates derived from radar can lead to errors in the estimates of detection and false alarm rates. These can be significant if: (a) the deforestation rate is

small and comparable to error rates in the Landsat classification; (b) there are appreciable differences in the intervals between which the Landsat data are gathered and those for the radar data. In this study, the detection rate inferred for FBD data is probably underestimated, but the false alarm rate is likely to be accurate.

8. All the analysis in the paper uses fully automatic methods, but it is likely that false alarms in the ScanSAR data due to periodic flooding could be reduced by human inspection. A semi-automated approach that exploits human knowledge may further improve performance, particularly with ScanSAR, since visual perception of areas of change may be able to out-perform significantly the pixel-based approaches used in the automatic processing. The performance figures reported here could also be improved if knowledge about the locations of dry and swampy forest was included in the methodology.

In this paper we have only considered the Riau region of Sumatra, and to realise the full significance of this work it is important to apply and test these methods in other tropical forests, both in Sumatra and in other parts of the tropics, including other parts of Indonesia, but also Africa and S. America. A key issue is then ancillary data to test performance; here we have benefited enormously from the availability of the WWF databases, despite the problems in using them consistently with the radar data discussed in Section 5. Extending this work to other areas is therefore best done in collaboration with other groups able to provide independent deforestation estimates. It is also important to evaluate the computing, data and human resources needed to apply these methods over large regions, for example the whole of Sumatra, and to investigate the feasibility of doing this.

ALOS-PALSAR is not the sole sensor applicable for monitoring tropical deforestation, though confers considerable advantages, and it needs to be considered within the total global capability relevant to this task. A natural framework for this is provided by the GEO Forest Carbon Tracking (GEO-FCT; http://www.geo-fct.org/) initiative, and further testing and application of our work may perhaps be best placed within the GEO-FCT context. This fits well with GEO-FCT aspirations to contribute to the development of National Forest Monitoring and Carbon Accounting Systems. Such considerations strongly motivated the work reported here, which aims to ensure that the use of ALOS-PALSAR data in GEO-FCT is fully understood, well-founded, and applies optimal approaches with quantified limitations.

Appendix: The effect of time inconsistencies and errors in the WWF databases

In this paper, the reference data against which deforestation is assessed consists of the forest area found in the 2007 Landsat images at time t_0. This contains both true forest and non-forest erroneously classified as forest, so has area

$$A_{F0} = A_F\, P_L(F \mid F) + A_{NF}\, P_L(F \mid NF),$$

where $P_L(F \mid F)$ and $P_L(F \mid NF)$ denote the probability that a Landsat pixel is classified as forest, given that it is forest and non-forest respectively. We will write $A' = A_F\, P_L(F \mid F)$. At time t_3, when the second WWF database is formed, a fraction $f_D(t_0, t_3)$ of the forested area has been lost. The area taken to be deforested between times t_0 and t_3 is the portion of A_{F0} classified as non-forest at time t_3, which is given by:

$$A_{NF3} = A'\big((1 - f_D(t_0,t_3))P_L(NF \mid F) + f_D(t_0,t_3)\,P_L(NF \mid NF)\big) + A_{NF}\,P_L(F \mid NF)\,P_L(NF \mid NF).$$

Here $P_L(NF \mid F)$ and $P_L(NF \mid NF)$ denote the probability that a Landsat pixel is classified as non-forest given that it is forest and non-forest respectively.

The *true* probability of detection in the FBD data is the fraction of the forested area lost between times t_1 and t_2 (i.e. the times of the first and second FBD acquisitions respectively), while the *estimated* probability of detection, $\hat{P}_d$, is the fraction of A_{NF3} seen as deforested in the FBD data: this includes erroneous detections in both the non-forest (i.e. areas deforested before t_1 and non-forest incorrectly classified as forest at time t_0), and in the forest which is undisturbed at time t_2. Hence the area indicated as deforested within the databases and detected as deforested using the FBD data is given by

$$A_{NFDF} = P_d\, A'\, f_D(t_1,t_2)\, P_L(NF \mid NF) + P_{fa}\, A'\big(f_D(t_2,t_3)\, P_L(NF \mid NF) + (1 - f_D(t_0,t_3))P_L(NF \mid F)\big) + P_p(DF \mid NF)\big(A'\, f_D(t_0,t_1)\, P_L(NF \mid NF) + A_{NF}\, P_L(F \mid NF)\, P_L(NF \mid NF)\big)$$

Here we have assumed that the detection and false alarm probabilities for FBD are independent of the classification probabilities for Landsat. Therefore

$$\hat{P}_d = A_{NFDF} / A_{NF3} = \frac{P_d\, f_D(t_1,t_2) + P_{fa}\big(f_D(t_2,t_3) + (1 - f_D(t_0,t_3))Y\big) + P_p(DF \mid NF)\big(f_D(t_0,t_1) + X\big)}{X + Y + f_D(t_0,t_3)(1-Y)}$$

where $f_D(t_i,t_j)$ is the fraction of the forest area deforested between times t_i and t_j, $P_p(DF \mid NF)$ is the probability that a pixel that is non-forest on both the acquisition dates of of the FBD data is detected as deforestation, and

$$X = \frac{A_{NF} P_L(F \mid NF)}{A_F P_L(F \mid F)} = \frac{A_{NF} P_L(F \mid NF)}{A'}$$

$$Y = \frac{P_L(NF \mid F)}{P_L(NF \mid NF)}.$$

The estimated probability of false alarm, $\hat{P}_{fa}$, is given by the fraction of A_{F0} that is classified as forest using Landsat at time t_3, A_{F3}, and as deforested by FBD, where

$$A_{F3} = A_{F0} - A_{NF3} = A'\big(P_L(F \mid F) + f_D(t_0,t_3)\big(P_L(F \mid NF) - P_L(F \mid F)\big)\big) + A_{NF}\, P_L(F \mid NF)\, P_L(F \mid NF)$$

The area within A_{F3} that is detected as deforested using FBD is

$$A_{FDF} = P_d\, A'\, f_D(t_1,t_2)\, P_L(F \mid NF) + P_{fa}\, A'\big(f_D(t_2,t_3)\, P_L(F \mid NF) + (1 - f_D(t_0,t_3))P_L(F \mid F)\big) + P_p(DF \mid NF)\big(A'\, f_D(t_0,t_1)\, P_L(F \mid NF) + A_{NF}\, P_L(F \mid NF)\, P_L(F \mid NF)\big)$$

Hence

$$\hat{P}_{fa} = A_{FDF} / A_{F3} = \frac{P_d\, f_D(t_1,t_2) V + P_{fa}\big(1 - f_D(t_0,t_3) + f_D(t_2,t_3) V\big) + P_p(DF \mid NF)\big(f_D(t_0,t_1) + X\big)V}{1 + XV + f_D(t_0,t_3)(V-1)}$$

where

$$V = \frac{P_L(F \mid NF)}{P_L(F \mid F)}.$$

Acknowledgements

This work was carried out with the support of the ALOS Kyoto & Carbon Initiative, (http://www.eorc.jaxa.jp/ALOS/en/kyoto/kyoto_index.htm) which is an international initiative led by the JAXA Earth Observation Research Centre (EORC), set up to support data

and information needs raised by international environmental conventions, carbon cycle science and conservation of the environment. We thank Sue Page, Kevin Tansey and Matt Waldram from the Dept of Geography at Leicester University for helpful discussions, and Francesca Ticconi (currently at DLR, Germany) for help and advice in the early stages of this project.

References

Achard, F., Eva, H.D., Stibig, H.-J., Mayaux, P., Gallego, J., Richards, T., & Malingreau, J.-P. (2002). Determination of Deforestation Rates of the World's Humid Tropical Forests. *Science, 297*, 999-1002

Angelis, C.F., Freitas, C.C., Valeriano, D.M., & Dutra, L.V. (2002). Multitemporal analysis of land use/land cover JERS-1 backscatter in the Brazilian tropical rainforest. *International Journal of Remote Sensing, 23*, 1231-1240

FAO (2010). Global Forest Resource Assessment 2010. In. Rome: Food and Agriculture Organization of the United Nations

Fuller, D.O. (2006). Tropical forest monitoring and remote sensing: A new era of transparency in forest governance? *Singapore Journal of Tropical Geography, 27*, 15-29

Ginn, C.M.R., Willett, P., & Bradshaw, J. (2000). Combination of molecular similarity measures using data fusion. *Perpectives in Drug Discovery and Design, 20*, 1-16

Goetz, S.J., Baccini, A., Laporte, N.T., Johns, T., Walker, W., Kelindorfer, J., Houghton, R.A., & Sun, M. (2009). Mapping and monitoring carbon stocks with satellite observations: a comparison of methods. In, *Carbon Balance and Management* (p. 2): BioMed Central Ltd

Hais, M., Jonášová, M., Langhammer, J., & Kučera, T. (2009). Comparison of two types of forest disturbance using multitemporal Landsat TM/ETM+ imagery and field vegetation data. *Remote sensing of environment, 113*, 835–845

Hansen, M.C., Stehman, S.V., Potapov, P.V., Arunarwati, B., Stolle, F., & Pittman, K.W. (2009). Quantifying changes in the rates of forest clearing in Indonesia from 1990 to 2005 using remotely sensed data sets. *Environmental Research Letters, 4*, 034001

Hansen, M.C., Stehman, S.V., Potapov, P.V., Loveland, T.R., Townshend, J.R.G., DeFries, R.S., Pittman, K.W., Arunarwati, B., Stolle, F., Steininger, M.K., Carroll, M., & DiMiceli, C. (2008). Humid tropical forest clearing from 2000 to 2005 quantified by using multitemporal and multiresolution remotely sensed data. *Proceedings of the National Academy of Sciences of the United States of America, 105*, 9439–9444

Holliday, J.D., Salim, N., Whittle, M., & Willett, P. (2003). Analysis and Display of the Size Dependence of Chemical Similarity Coefficients. *Journal of Chemical Information and Computer Science, 43*, 819-828

Houghton, R.A. (2005a). Aboveground Forest Biomass and the Global Carbon Balance. *Global Change Biology, 11*, 945-958

Houghton, R.A. (2005b). Tropical deforestation as a source of greenhouse gas emissions. In P. Moutinho, & S. Schwartzman (Eds.), *Tropical Deforestation and Climate Change* (pp. 13-21). Washington DC - USA: Amazon Institute for Environmental Research (IPAM)

Houghton, R.A., Skole, D.L., Nobre, C.A., Hackler, J.L., Lawrence, K.T., & Chomentowski, W.H. (2000). Annual fluxes of carbon from deforestation and regrowth in the Brazilian Amazon. *Nature, 403*, 301

Le Quéré, C. (2010). Trends in the land and ocean carbon uptake. *Current Opinion in Environmental Sustainability, 2*, 219-224

Leckie, D.G., & Ranson, J.K. (1998). Chapter 9 - Forestry Applications Using Imagng Radar. In R.A. Ryerson (Ed.), *Manual of remote sensing. Vol.2, Principles and applications of imaging radar / edited by Floyd M. Henderson and Anthony J. Lewis.* New York; Chichester: J. Wiley

Martinez, J.M., & Le Toan, T. (2007). Mapping of flood dynamics and spatial distribution of vegetation in the Amazon floodplain using multitemporal SAR data. *Remote sensing of environment, 108*, 209-233

Parker, C., Mitchell, A., Tivedi, M., & Mardas, N. (2009). The Little REDD+ Book. In, *An updated guide to governmental and non-governmental proposals for reducing emissions from deforestation and degradation.*: Global Canopy Programme, John Krebs Field Station, Oxford OX2 8QJ, UK

Podest, E., & Saatchi, S. (2002). Application of multiscale texture in classifying JERS-1 radar data over tropical vegetation. *International Journal of Remote Sensing, 23*, 1487-1506

Quegan, S., LeToan, T., Yu, J.J., Ribbes, F., & Floury, N. (2000). Multitemporal ERS SAR Analysis Applied to Forest Mapping. *IEEE Transactions on Geoscience and Remote Sensing*

Quegan, S., & Yu, J.J. (2001). Filtering of Multichannel SAR images. *IEEE Transactions on Geoscience and Remote Sensing, 39*, 2373-2379

Rignot, E.J.M., & van Zyl, J.J. (1993). Change detection techniques for ERS-1 SAR data. *IEEE Transactions on Geoscience and Remote Sensing, 31*, 896-906

Rosenqvist, A., Shimada, M., Ito, N., & Watanabe, M. (2007). ALOS PALSAR: A Pathfinder Mission fo Global-Scale Monitoring of the Environment. *IEEE Transactions on Geoscience and Remote Sensing, 45*, 3307-3316

Stone, T.A., & Woodwell, G.M. (1988). Shuttle imaging radar A analysis of land use in Amazonia. *International Journal of Remote Sensing, 9*, 95-105

Touzi, R., Lopes, A., & Bousquet, P. (1988). A statistical and geometrical edge detector for SAR images. *IEEE Transactions on Geoscience and Remote Sensing, 26*, 764-773

UNFCCC (2007). Report of the Conference of the Parties on its Thirteenth Session. In, *The United Nations Climate Change Conference.* Bali

UNFCCC (2011). Fact sheet: Reducing emissions from deforestation in developing countries: approaches to stimulate action. In

Uryu, Y., Mott, C., Foead, N., Yulianto, K., Budiman, A., Setiabudi, Takakai, F., Nursamsu, Sunarto, Purastuti, E., Fadhli, N., Hutajulu, C.M.B., Jaenicke, J., Hatano, R., Siegert, F., &

Stüwe, M. (2007). Deforestation, Forest Degradation, Biodiversity Loss and CO2 Emissions in Riau, Sumatra, Indonesia. WWF Indonesia Technical Report. In. Jakarta, Indonesia

Uryu, Y., Purastuti, E., Laumonier, Y., Budiman, A., Yulianto, K., Sudibyo, A., Hadian, O., Kosasih, D.A., & Stüwe, M. (2010). Sumatra's Forests, their Wildlife and the Climate. Windows in Time: 1985, 1990, 2000 and 2009. In. Jakarta, Indonesia: WWF-Indonesia

Whittle, M., Gillett, V.J., Willett, P., Alex, A., & Loesel, J. (2004). Enhancing the Effectiveness of Virtual Screening by Fusing Nearest Neighbor Lists: A Comparison of Similarity Coefficients. *Journal of Chemical Information and Computer Science, 44*, 1840-1848